Draft version December 30, 2015
Preprint typeset using LaTeX style emulateapj v. 2/16/10

arXiv:1201.0659v2 [astro-ph.EP] 5 Apr 2012

HAT-P-34b — HAT-P-37b: FOUR TRANSITING PLANETS MORE MASSIVE THAN JUPITER ORBITING MODERATELY BRIGHT STARS†

G. Á. Bakos[1,2,⋆], J. D. Hartman[1,2], G. Torres[2], B. Béky[2], D. W. Latham[2], L. A. Buchhave[3], Z. Csubry[1,2], G. Kovács[4], A. Bieryla[2], S. Quinn[2], T. Szklenár[2], G. A. Esquerdo[2], A. Shporer[5], R. W. Noyes[2], D. A. Fischer[6], J. A. Johnson[7], A. W. Howard[8], G. W. Marcy[8], B. Sato[9], K. Penev[1,2], M. Everett[2], D. D. Sasselov[2], G. Fűrész[2], R. P. Stefanik[2], J. Lázár[10], I. Papp[10] & P. Sári[10]

Draft version December 30, 2015

ABSTRACT

We report the discovery of four transiting extrasolar planets (HAT-P-34b–HAT-P-37b) with masses ranging from 1.05 to 3.33 M_J and periods from 1.33 to 5.45 days. These planets orbit relatively bright F and G dwarf stars (from $V = 10.16$ to $V = 13.2$). Of particular interest is HAT-P-34b which is moderately massive (3.33 M_J), has a high eccentricity of $e = 0.441 \pm 0.032$ at $P = 5.452654 \pm 0.000016\,d$ period, and shows hints of an outer component. The other three planets have properties that are typical of hot Jupiters.

Subject headings: planetary systems — stars: individual (HAT-P-34, GSC 1622-01261, HAT-P-35, GSC 0203-01079, HAT-P-36, GSC 3020-02221, HAT-P-37, GSC 3553-00723) techniques — spectroscopic, photometric

1. INTRODUCTION

Transiting extrasolar planets (TEPs) provide unique opportunities to study the properties of planetary objects outside of the Solar System. To date well over 100 such planets have been discovered and characterized[13], leading to numerous insights into the physical properties of planetary systems (e.g. see the recent review by Rauer 2011). In addition, over a thousand strong candidates from *Kepler* have been identified (Borucki et al. 2011), greatly expanding our understanding of several aspects of planetary systems, such as the properties of multi-planet systems (Latham et al. 2011; Lissauer et al. 2011), and the distribution of planetary radii (Howard et al. 2011). However, due to the large number of important variables which influence the physical properties of a planet (e.g. its mass, composition, age, irradiation, and tides, to name a few), we are still far from an empirically tested, comprehensive understanding of the formation and evolution of planetary systems.

Here we present the discovery of four new TEPs identified by the Hungarian-made Automated Telescope Network (HATNet; Bakos et al. 2004) survey which contribute to the rapidly-growing sample of TEPs. These planets transit relatively bright stars facilitating detailed characterization of their properties, such as measurements of their masses via radial velocity (RV) observations of the host star, or measuring their orbital tilt via the Rossiter-McLaughlin effect.

The HATNet survey for TEPs around bright stars ($9 \lesssim r \lesssim 14.5$) operates six wide-field instruments: four at the Fred Lawrence Whipple Observatory (FLWO) in Arizona (HAT-5, -6, -7, and -10), and two on the roof of the hangar servicing the Smithsonian Astrophysical Observatory's Submillimeter Array, in Hawaii (HAT-8 and -9). Since 2006, HATNet has announced and published 33 TEPs (e.g. Johnson et al. 2011). In this work we report our thirty-fourth through thirty-seventh discoveries, around the stars GSC 1622-01261, GSC 0203-01079, GSC 3020-02221, and GSC 3553-00723.

In Section 2 we summarize the detection of the photometric transit signals and the subsequent spectroscopic and photometric observations of each star to confirm the planets. In Section 3 we analyze the data to determine the stellar and planetary parameters. The properties of these planets are briefly discussed in Section 4.

2. OBSERVATIONS

The observational procedure employed by HATNet to discover TEPs has been described in detail in several previous discovery papers (e.g. Bakos et al. 2010; Latham et al. 2009). In the following subsections we highlight specific details of this procedure that are per-

[1] Department of Astrophysical Sciences, Princeton University, Princeton, NJ 08544; email: gbakos@astro.princeton.edu
[2] Harvard-Smithsonian Center for Astrophysics
[3] Niels Bohr Institute, University of Copenhagen, DK-2100, Denmark, and Centre for Star and Planet Formation, Natural History Museum of Denmark, DK-1350 Copenhagen
[4] Konkoly Observatory, Budapest, Hungary
[5] LCOGT, 6740 Cortona Drive, Santa Barbara, CA, & Department of Physics, Broida Hall, UC Santa Barbara, CA
[6] Astronomy Department, Yale University, New Haven, CT
[7] California Institute of Technology, Department of Astrophysics, MC 249-17, Pasadena, CA
[8] Department of Astronomy, University of California, Berkeley, CA
[9] Department of Earth and Planetary Sciences, Tokyo Institute of Technology, 2-12-1 Ookayama, Meguro-ku, Tokyo 152-8551, Japan
[10] Hungarian Astronomical Association, Budapest, Hungary
⋆ Alfred. P. Sloan Research Fellow.
† Based in part on observations obtained at the W. M. Keck Observatory, which is operated by the University of California and the California Institute of Technology. Keck time has been granted by NOAO (A289Hr) and NASA (N167Hr, N029Hr). Based in part on data collected at Subaru Telescope, which is operated by the National Astronomical Observatory of Japan. Based in part on observations made with the Nordic Optical Telescope, operated on the island of La Palma jointly by Denmark, Finland, Iceland, Norway, and Sweden, in the Spanish Observatorio del Roque de los Muchachos of the Instituto de Astrofisica de Canarias.
[13] See e.g. http://exoplanets.org (Wright et al. 2011) for the list of published planets, or www.exoplanet.eu (Schneider et al. 2011) for a more extended compilation, including unpublished results.

TABLE 1
Summary of discovery data.

Planet Host	GSC	2MASS	RA HH:MM:SS	DEC DD:MM:SS	V[a] mag	Depth[b] mmag	Period days
HAT-P-34	1622-01261	20124688+1806175	$20^{h}12^{m}46.80s$	$+18°06'17.5''$	10.162 ± 0.073	7.9	5.4527
HAT-P-35	0203-01079	08130018+0447132	$08^{h}13^{m}00.19s$	$+04°47'13.3''$	12.46 ± 0.11	9.0	3.6467
HAT-P-36	3020-02221	12330390+4454552	$12^{h}33^{m}03.96s$	$+44°54'55.3''$	12.262 ± 0.068	14.7	1.3273
HAT-P-37	3553-00723	18571105+5116088	$18^{h}57^{m}11.16s$	$+51°16'08.9''$	13.23 ± 0.32[c]	18.1	2.7974

[a] From Droege et al. 2006.
[b] Note that the apparent depth of the HATNet transit for all four targets is shallower than the true transit depth due to blending with unresolved neighbors in the low spatial resolution HATNet images (the median full-width at half maximum of the point-spread function at the center of a HATNet image is $\sim 25''$). Also, we applied the trend filtering procedure in non signal-reconstructive mode, which reduces the transit depth while increasing the signal-to-noise ratio of the detection. For each system the ratio of the planet and stellar radii, which is related to the true transit depth, is determined in Section 3.2 using the higher spatial-resolution photometric follow-up observations described in Section 2.4.
[c] From Lasker et al. 2008.

tinent to the discoveries of the four planets presented in this paper.

2.1. *Photometric detection*

Table 2 summarizes the HATNet discovery observations of each new planetary system. The HATNet images were processed and reduced to trend-filtered light curves following the procedure described by Bakos et al. (2010) and Pál (2009b). The light curves were searched for periodic box-shaped signals using the Box Least-Squares (BLS; see Kovács et al. 2002) method. We detected significant signals in the light curves of the stars summarized in Table 1.

2.2. *Reconnaissance Spectroscopy*

High-resolution, low-S/N "reconnaissance" spectra were obtained for HAT-P-34 and HAT-P-35 using the Tillinghast Reflector Echelle Spectrograph (TRES; Fűrész 2008) on the 1.5 m Tillinghast Reflector at FLWO. These observations were reduced and analyzed following the procedure described by Quinn et al. (2010) and Buchhave et al. (2010); the results are listed in Table 3. For both objects the spectra were single-lined, and showed radial velocity (RV) variations on the order of $\sim 100\,\mathrm{m\,s^{-1}}$. Proper phasing of the RV with the photometric ephemeris gives confidence in acquiring further, high signal-to-noise spectroscopic observations to refine the orbit (see § 2.3). While for HAT-P-34 the variations initially did not appear to phase with the photometric ephemeris, we entertained the possibility of a very significant non-zero eccentricity, and pursued follow-up of the target. For HAT-P-35 the variations were in phase with the photometric ephemeris indicating a $\sim 2.7\,M_{\rm J}$ companion. For both HAT-P-36 and HAT-P-37 we obtained two TRES spectra near each of the predicted quadrature phases. For both objects the spectra were single-lined. For HAT-P-36 the resulting RV measurements showed $\sim 400\,\mathrm{m\,s^{-1}}$ variation in phase with the photometric ephemeris, while for HAT-P-37 the RV measurements showed $\sim 260\,\mathrm{m\,s^{-1}}$ variation in phase with the ephemeris. We opted to continue observing both of these objects using TRES with the aim of confirming the planets. The TRES observations of HAT-P-36 and HAT-P-37 are discussed further in the following subsection.

2.3. *High resolution, high S/N spectroscopy*

We proceeded with the follow-up of each candidate by obtaining high-resolution, high-S/N spectra to characterize the RV variations, and to refine the determination of the stellar parameters. These observations are summarized in Table 4. The RV measurements and uncertainties for HAT-P-34 through HAT-P-37 are given in the Appendix, and in Tables 7–10, respectively. The period-folded data, along with our best fit described below in Section 3, are displayed in Figures 2–5.

Four facilities were used in the confirmation of these planets (including three separate facilities used for HAT-P-34). These facilities are HIRES (Vogt et al. 1994) on the 10 m Keck I telescope in Hawaii, the High-Dispersion Spectrograph (HDS; Noguchi et al. 2002) on the 8.3 m Subaru telescope in Hawaii, the FIbre-fed Échelle Spectrograph (FIES) on the 2.5 m Nordic Optical Telescope (NOT) at La Palma, Spain (Djupvik & Andersen 2010), and TRES on the FLWO 1.5 m telescope.

The HIRES and HDS observations made use of the iodine-cell method (Marcy & Butler 1992; Butler et al. 1996) for precise wavelength calibration and relative RV determination, while the FIES and TRES observations made use of Th-Ar lamp spectra obtained before and after the science exposures. The HIRES observations were reduced to relative RVs in the barycentric frame following Butler et al. (1996), Johnson et al. (2009), and Howard et al. (2010), the HDS observations were reduced following Sato et al. (2002, 2005), and the FIES and TRES observations were reduced following Buchhave et al. (2010).

We found that for all four systems the RV residuals from the best-fit models, described below in Section 3.2, exhibit excess scatter over what is expected based on the formal measurement uncertainties. Such excess scatter, or "jitter" has been well known for stars, and can stem for multiple sources. The excess is in the residuals of the observations with respect to a physical (and possibly instrumental) model. If this model is not adequate, the residuals can be larger than expected. For example, in the case of HAT-P-34b, ignoring the linear trend in the RVs would lead to a much increased "jitter". Additional planets may cause jitter, as the limited number of RV observations is not enough to uniquely identify and model such systems. The typical source of the jitter, however, is the star itself, namely inhomogeneities (spots, flares, plages, etc.) on the stellar surface (e.g. Makarov et al. 2009; Martínez-Arnáiz et al. 2010) causing jitters up to

TABLE 2
Summary of photometric observations

Instrument/Field	Date(s)	Number of Images	Cadence (sec)	Filter
HAT-P-34				
HAT-7/G293	2008 Oct–2009 May	755	330	r
HAT-8/G293	2008 Sep–2008 Dec	2611	330	r
HAT-6/G341	2007 Sep–2007 Dec	1949	330	R
HAT-9/G341	2007 Sep–2007 Nov	2379	330	R
KeplerCam	2010 May 21	263	60	z
KeplerCam	2010 Oct 10	530	30	i
HAT-P-35				
HAT-5/G364	2009 May	21	330	r
HAT-9/G364	2008 Dec–2009 May	3155	330	r
KeplerCam	2011 Jan 16	110	100	i
FTN	2011 Jan 23	185	45	i
KeplerCam	2011 Mar 08	268	60	i
HAT-P-36				
HAT-5/G143	2010 Apr–2010 Jul	4471	210	r
HAT-8/G143	2010 Apr–2010 Jul	6262	210	r
KeplerCam	2010 Dec 24	131	130	i
KeplerCam	2011 Feb 03	101	100	i
KeplerCam	2011 Feb 07	105	100	i
KeplerCam	2011 Feb 15	186	60	i
HAT-P-37				
HAT-7/G115	2009 Sep–2010 Jul	7102	210	r
HAT-9/G115	2008 Aug–2008 Sep	2293	330	R
KeplerCam	2011 Feb 23	37	165	i
KeplerCam	2011 Mar 23	73	134	i
KeplerCam	2011 Apr 06	102	134	i

TABLE 3
Summary of reconnaissance spectroscopy observations[a]

Instrument	HJD	$\gamma_{\rm RV}$[b] ($\rm km\,s^{-1}$)	CC Peak[c]
HAT-P-34			
TRES	2454935.00839	−47.81	0.726
TRES	2454966.97204	−49.19	0.939
TRES	2454998.97956	−49.12	0.819
HAT-P-35			
TRES	2455289.64284	41.24	0.863
TRES	2455291.62482	40.54	0.883
TRES	2455320.64182	40.83	0.935
TRES	2455321.64383	41.08	0.940

[a] For HAT-P-36 and HAT-P-37, which were confirmed using the TRES spectrograph, there is no clear distinction between reconnaissance and high-precision observations. We do not list the results from the analysis of the TRES spectra for these targets here, these are instead described in Section 2.3.
[b] The heliocentric RV of the target in the IAU system, and corrected for the orbital motion of the planet.
[c] The peak value of the cross-correlation function between the observed spectrum and the best-matching synthetic template spectrum (normalized to be between 0 and 1). Observations with a peak height closer to 1.0 generally correspond to higher S/N spectra.

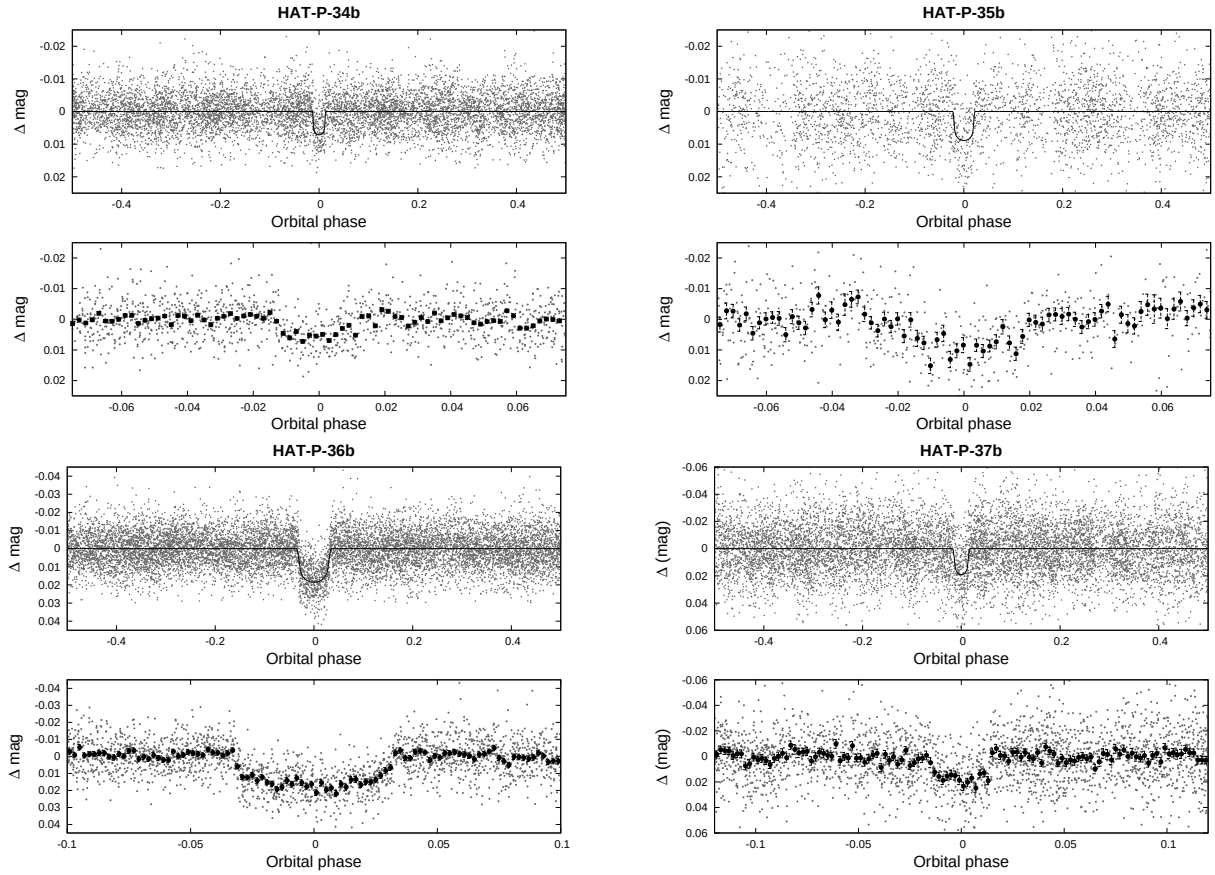

FIG. 1.— HATNet light curves of HAT-P-34 through HAT-P-37. See Table 2 for a summary of the observations. For each planet we show two panels. The top panel shows the unbinned light curve folded with the period resulting from the global fit described in Section 3. The solid line shows the model fit to the light curve (Section 3.2). The bottom panel shows the region zoomed-in on the transit. The dark filled circles show the light curve binned in phase with a binsize of 0.002.

100 ms. Granulation and stellar oscillations contribute at a smaller scale, but are present for non-active stars that are outside the instability strip. A recent publication by Cegla et al. (2012) discusses the stellar jitter due to variable gravitational redshift of the star, as the stellar radius changes due to oscillations (ΔR of 10^{-4} causing $\sim 0.1\,\mathrm{m\,s^{-1}}$). And, of course, systematics in the instrument further inflate the jitter. A review of RV jitter of stars observed by the Keck telescope are given in Wright (2005).

In order to ensure realistic estimates of the system parameter uncertainties we add in quadrature an RV jitter to the formal RV measurement uncertainties such that χ^2 per degree of freedom is unity for the best-fit model for each planet. We adopt an independent jitter for the observations made by each instrument of each planet. The RV uncertainties given in Tables 7–10 do *not* include this jitter; we do include the jitter in Figures 2–5.

For HAT-P-34 and HAT-P-35 we also show the S index, which is a measure of the chromospheric activity of the star derived from the flux in the cores of the Ca II H and K lines. This index was computed following Isaacson & Fischer (2010) and has been calibrated to the scale of Vaughan, Preston & Wilson (1978). A procedure for obtaining calibrated S index values from the TRES spectra has not yet been developed, so we do not provide these measurements for HAT-P-36 or HAT-P-37. We convert the S index values to $\log R'_{\mathrm{HK}}$ following Noyes et al. (1984) and find median values of $\log R'_{\mathrm{HK}} = -4.859$ and $\log R'_{\mathrm{HK}} = -5.242$ for HAT-P-34 and HAT-P-35, respectively. These values imply that neither star has a particularly high level of chromospheric activity.

Following Queloz et al. (2001) and Torres et al. (2007), we checked whether the measured radial velocities are not real, but are instead caused by distortions in the spectral line profiles due to contamination from a nearby unresolved eclipsing binary. A bisector (BS) analysis for each system based on the Keck and TRES spectra was done as described in §5 of Bakos et al. (2007a). For HAT-P-35, which is relatively faint, we found that the measured BSs were significantly affected by scattered moonlight and applied an empirical correction for this effect following Hartman et al. (2009) (see also Kovács et al. (2010)). For HAT-P-34 the BS scatter is fairly high ($\sim 25\,\mathrm{m\,s^{-1}}$), but this is in line with the high RV jitter ($\sim 60\,\mathrm{m\,s^{-1}}$), which is typical of an F star with $v \sin i = 24.0 \pm 0.5\,\mathrm{km\,s^{-1}}$ (Saar et al. 2003; Hartman et al. 2011b).

None of the systems show significant bisector span variations (relative to the semi-amplitude of the RV variations) that phase with the photometric ephemeris. Such variations are generally expected if the transit and RV signals were due to blends rather than planets. While the lack of bisector span variations does not exclude *all* blend scenarios, it does significantly limit the possible blend scenarios that can reproduce our current data within the measurement errors, i.e. configurations that are compatible with the photometric and spectroscopic observations, proper motions, color indices, and moderately high resolution imaging. We have found in the past that invoking detailed blend modeling to exclude all possible blend configurations and confirm the planet hypothesis (e.g. Hartman et al. 2011a, sections 3.2.2, 3.2.3) is rarely of any incremental value when the ingress and egress dura-

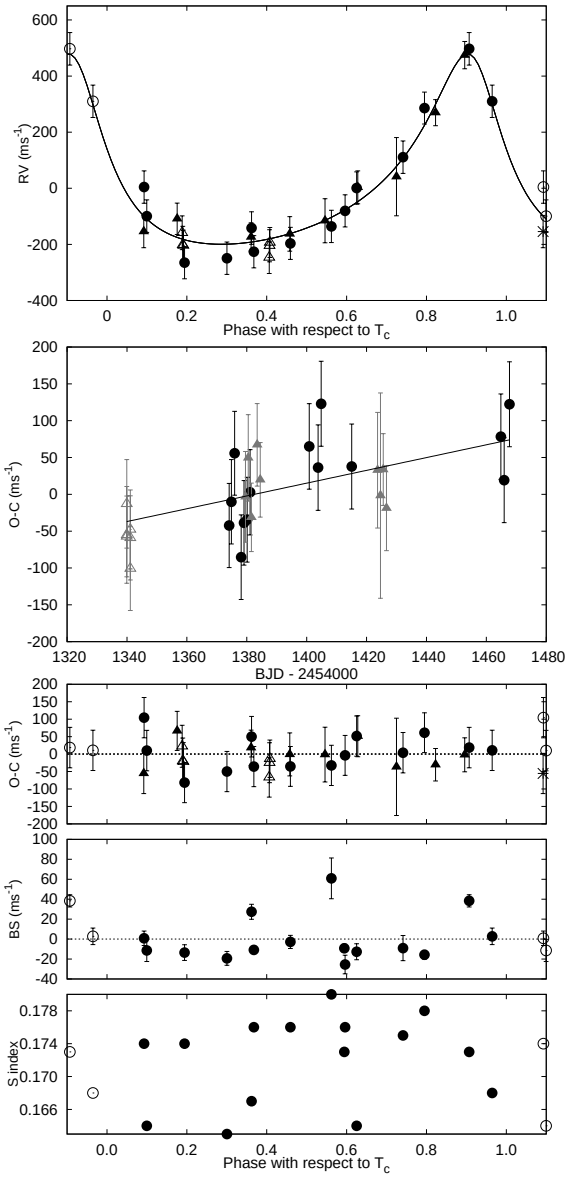

FIG. 2.— *Top panel:* High-precision RV measurements for HAT-P-34 shown as a function of orbital phase, along with our best-fit model (see Table 6). Open triangles show measurements from Subaru/HDS, filled circles show measurements from Keck/HIRES, and filled triangles show measurements from NOT/FIES. Zero phase corresponds to the time of mid-transit. The center-of-mass velocity and a linear trend have been subtracted. *Second panel:* velocity $O-C$ residuals from the best-fit single Keplerian orbit model as a function of time. The residuals show a slight linear trend, possibly indicating a third body in the system. Note that the zero-points of the three separate instruments are independently free parameters. *Third panel:* velocity $O-C$ residuals from the best fit including both the Keplerian orbit and linear trend, shown as a function of orbital phase. The error bars include a jitter term ($56.0\,\mathrm{m\,s^{-1}}$ for the Keck/HIRES observations, and $32.0\,\mathrm{m\,s^{-1}}$ for the Subaru/HDS observations; no jitter has been added to the NOT/FIES RV uncertainties) added in quadrature to the formal errors (see Section 3.2). *Fourth panel:* bisector spans (BS) from Keck/HIRES, with the mean value subtracted. The measurement from the template spectrum is included. *Bottom panel:* Chromospheric activity index S measured from the Keck spectra. Note the different vertical scales of the panels. Observations shown twice are represented with open symbols.

TABLE 4
Summary of high-SN spectroscopic observations used in measuring the orbits

Instrument	Date(s)	Number of RV obs.
HAT-P-34		
Subaru/HDS	2010 May	6
Keck/HIRES	2010 Jun–2010 Sep	14
NOT/FIES	2010 Jul–2010 Aug	10
HAT-P-35		
Keck/HIRES	2010 Sep–2010 Dec	7
NOT/FIES	2010 Oct	5[a]
HAT-P-36		
FLWO 1.5/TRES	2010 Dec–2011 Jan	12
HAT-P-37		
FLWO 1.5/TRES	2011 Mar–2011 May	13

[a] One of the NOT/FIES spectra of HAT-P-35 was aborted early due to morning twilight and high humidity, another exposure was obtained partly during transit and may be affected by the Rossiter-McLaughlin effect. The remaining three NOT/FIES spectra do not provide sufficient phase coverage to constrain the orbit. We therefore do not include the velocities measured from these spectra in the analysis of HAT-P-35.

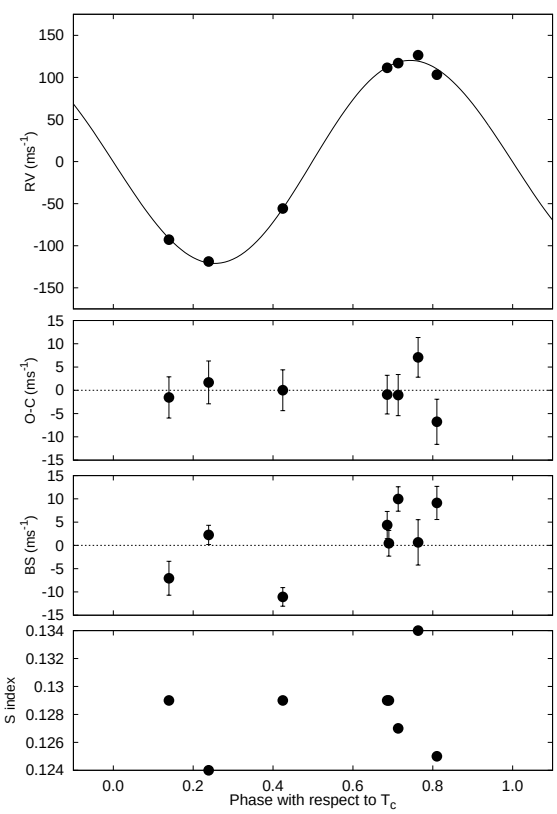

Fig. 3.— Keck/HIRES observations of HAT-P-35. The panels are as in Figure 2. The parameters used in the best-fit model are given in Table 6.

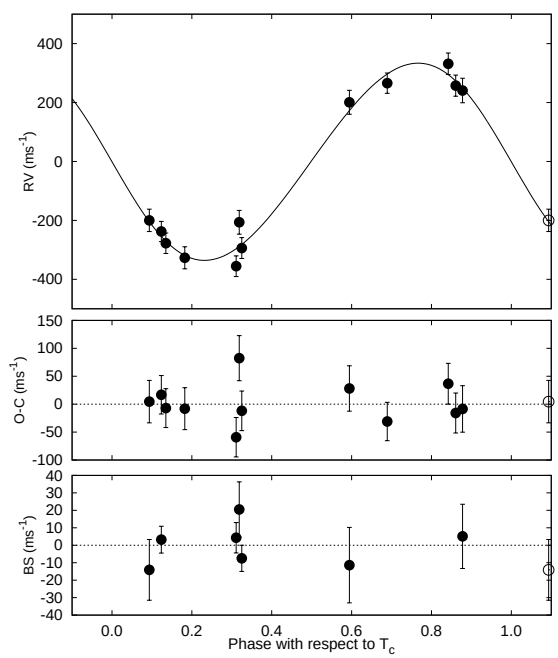

Fig. 4.— FLWO 1.5 m/TRES observations of HAT-P-36. The panels are as in Figure 2. The S index is not available for these observations. The parameters used in the best-fit model are given in Table 6.

tions are short relative to the total transit duration, the RV variations exhibit a Keplerian orbit in phase with the photometric ephemeris, and bisector spans show no correlation with the orbit. We conclude that the velocity variations detected for all four stars are real, and that each star is orbited by a close-in giant planet.

2.4. *Photometric follow-up observations*

In order to permit a more accurate modeling of the light curves, we conducted additional photometric observations using the KeplerCam CCD camera on the FLWO 1.2 m telescope, and the Spectral Instrument CCD on the 2.0 m Faulkes Telescope North (FTN) at Haleakala Observatory in Hawaii, which is operated by the Las Cumbres Observatory Global Telescope (LCOGT). The observations for each target are summarized in Table 2.

The reduction of these images was performed as de-

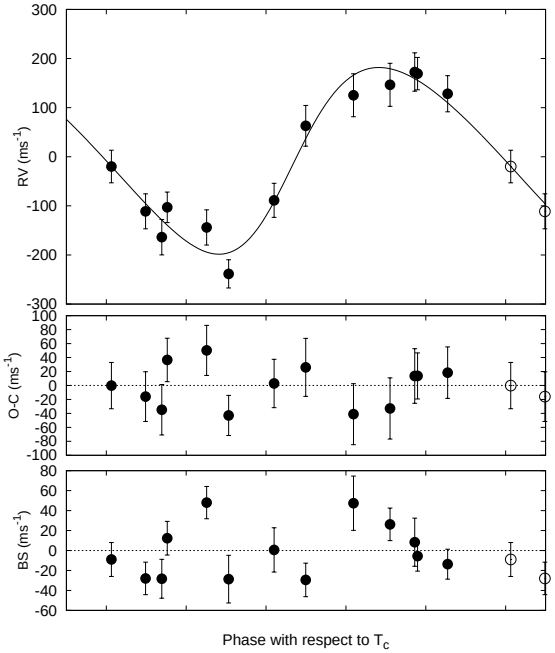

FIG. 5.— FLWO 1.5 m/TRES observations of HAT-P-37. The panels are as in Figure 2. The S index is not available for these observations. The parameters used in the best-fit model are given in Table 6.

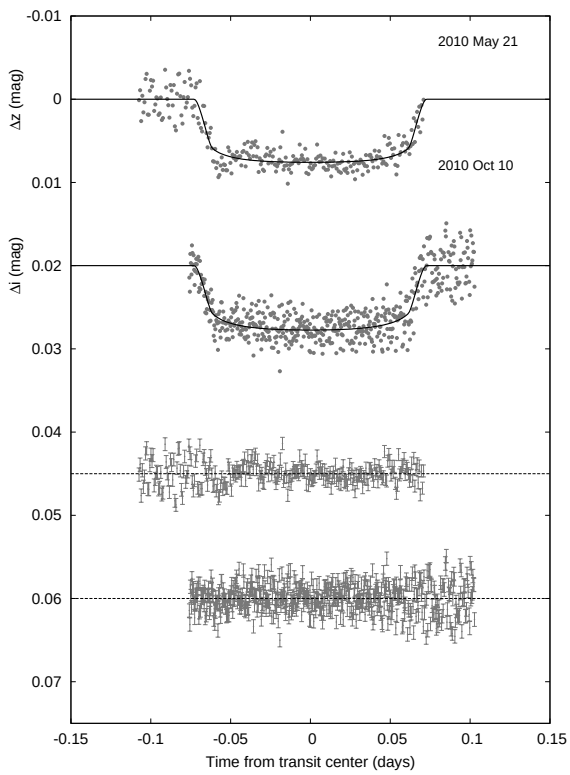

FIG. 6.— Unbinned transit light curves for HAT-P-34, acquired with KeplerCam at the FLWO 1.2 m telescope. The light curves have been EPD- and TFA-processed, as described in § 3.2. The dates of the events are indicated. Curves after the first are displaced vertically for clarity. Our best fit from the global modeling described in Section 3.2 is shown by the solid lines. Residuals from the fits are displayed at the bottom, in the same order as the top curves. The error bars represent the photon and background shot noise, plus the readout noise.

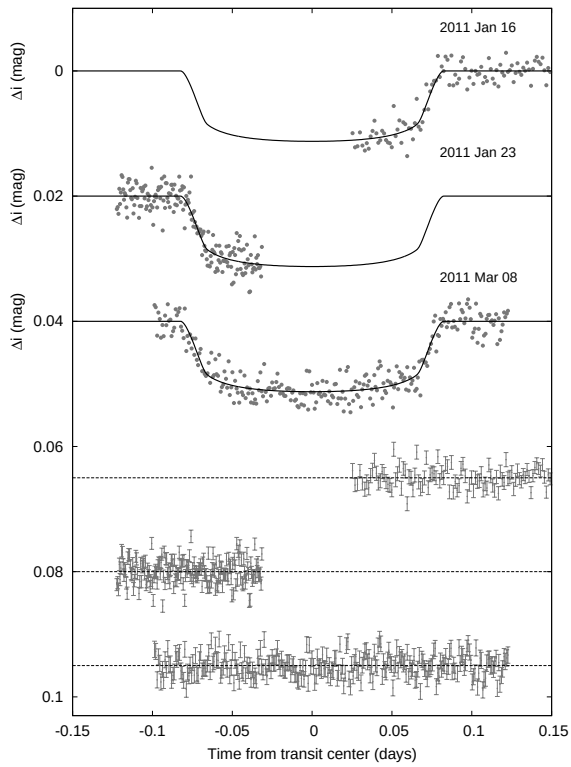

FIG. 7.— Similar to Figure 6; here we show the follow-up light curves for HAT-P-35.

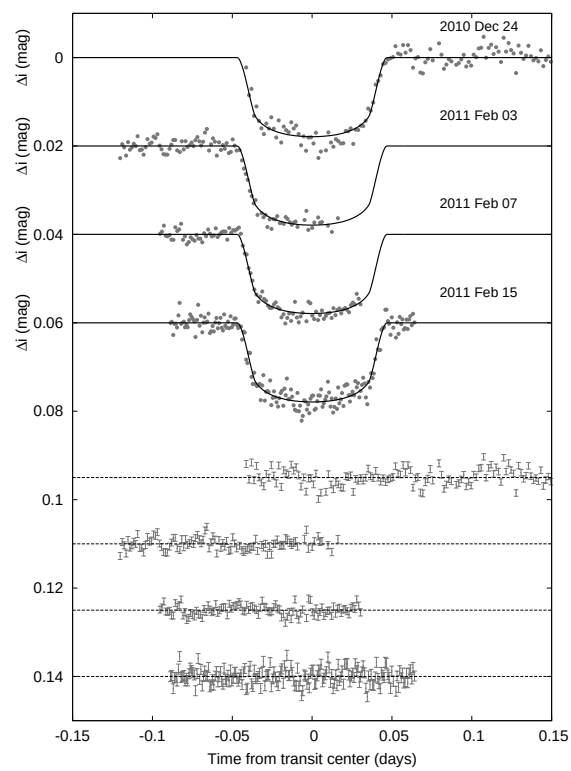

FIG. 8.— Similar to Figure 6; here we show the follow-up light curves for HAT-P-36.

scribed by Bakos et al. (2010). We applied External Parameter Decorrelation (EPD; Bakos et al. 2010) and the

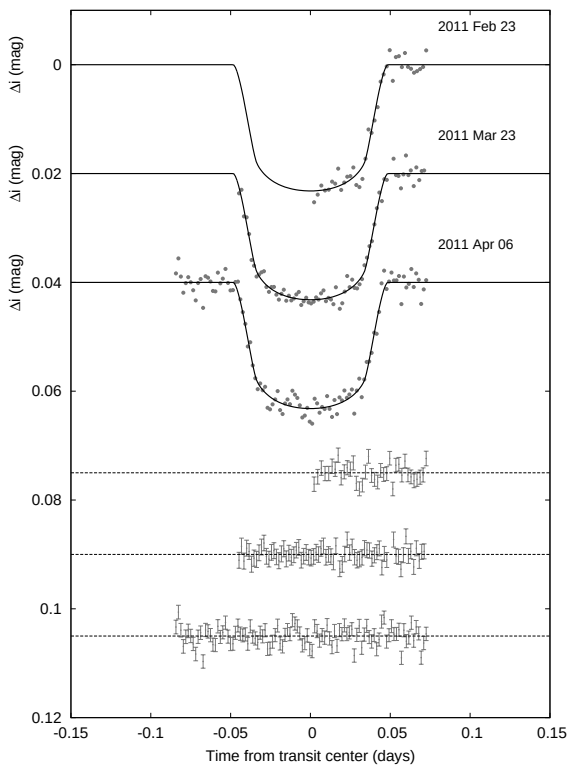

FIG. 9.— Similar to Figure 6; here we show the follow-up light curves for HAT-P-37.

Trend Filtering Algorithm (TFA; Kovács et al. 2005) to remove trends simultaneously with the light curve modeling. The final time series, together with our best-fit transit light curve models, are shown in the top portion of Figures 6–9 for HAT-P-34 through HAT-P-37, respectively. The individual measurements, permitting independent analysis by other researchers, are reported in the Appendix, in Tables 11–14 (the full data are available in electronic format).

3. ANALYSIS

3.1. *Properties of the parent star*

Stellar atmospheric parameters for HAT-P-34 and HAT-P-35 were measured using our template spectra obtained with the Keck/HIRES instrument, and the analysis package known as Spectroscopy Made Easy (SME; Valenti & Piskunov 1996), along with the atomic line database of Valenti & Fischer (2005). For HAT-P-36 and HAT-P-37 the stellar atmospheric parameters were determined by cross-correlating the TRES observations against a finely sampled grid of synthetic spectra based on Kurucz (2005) model atmospheres. This procedure, known as Stellar Parameter Classification (SPC), will be described in detail in a forthcoming paper (Buchhave et al., in preparation). We note that SPC has been performed in the past on numerous HATNet transiting planet candidates (Buchhave, personal communication), and the results were consistent with those of SME.

For each star, we obtained the following *initial* spectroscopic parameters and uncertainties:

- *HAT-P-34* – effective temperature $T_{\rm eff\star} = 6400 \pm 100\,{\rm K}$, metallicity $[{\rm Fe/H}] = +0.21 \pm 0.1\,{\rm dex}$, stellar surface gravity $\log g_\star = 3.98 \pm 0.1\,({\rm cgs})$, and projected rotational velocity $v \sin i = 24.5 \pm 1.0\,{\rm km\,s^{-1}}$.
- *HAT-P-35* – effective temperature $T_{\rm eff\star} = 5940 \pm 88\,{\rm K}$, metallicity $[{\rm Fe/H}] = +0.01 \pm 0.08\,{\rm dex}$, stellar surface gravity $\log g_\star = 3.98 \pm 0.1\,({\rm cgs})$, and projected rotational velocity $v \sin i = 0.5 \pm 0.5\,{\rm km\,s^{-1}}$.
- *HAT-P-36* – effective temperature $T_{\rm eff\star} = 5850 \pm 100\,{\rm K}$, metallicity $[{\rm Fe/H}] = +0.38 \pm 0.1\,{\rm dex}$, stellar surface gravity $\log g_\star = 4.73 \pm 0.17\,({\rm cgs})$, and projected rotational velocity $v \sin i = 2.86 \pm 0.5\,{\rm km\,s^{-1}}$.
- *HAT-P-37* – effective temperature $T_{\rm eff\star} = 5570 \pm 100\,{\rm K}$, metallicity $[{\rm Fe/H}] = +0.09 \pm 0.1\,{\rm dex}$, stellar surface gravity $\log g_\star = 4.67 \pm 0.1\,({\rm cgs})$, and projected rotational velocity $v \sin i = 2.95 \pm 0.5\,{\rm km\,s^{-1}}$.

Following Bakos et al. (2010), these initial values of $T_{\rm eff\star}$, $\log g_\star$, and [Fe/H] were used to determine the quadratic limb-darkening coefficients needed in the global modeling of the follow-up photometry (summarized in Section 3.2). This analysis yields $\rho_\star$, the mean stellar density, which is closely related to $a/R_\star$, the normalized semimajor axis, and provides a tighter constraint on the stellar parameters than does the spectroscopically determined $\log g_\star$ (e.g. Sozzetti et al. 2007). We combined $\rho_\star$, $T_{\rm eff\star}$, and [Fe/H] with stellar evolution models from the Yonsei-Yale (YY) series by Yi et al. (2001) to determine probability distributions of other stellar properties, including $\log g_\star$. For each system we carried out a second SME or SPC iteration in which we adopted the new value of $\log g_\star$ so determined and held it fixed in a new SME or SPC analysis, adjusting only $T_{\rm eff\star}$, [Fe/H], and $v \sin i$, followed by a second global modeling of the RV and light curves, together with improved limb darkening parameters. The *final* atmospheric parameters that we adopt, together with stellar parameters inferred from the YY models (such as the mass, radius and age) are listed in Table 5 for all four stars.

The inferred location of each star in a diagram of $a/R_\star$ versus $T_{\rm eff\star}$, analogous to the classical H-R diagram, is shown in Figure 10. In each case the stellar properties and their 1σ and 2σ confidence ellipses are displayed against the backdrop of model isochrones for a range of ages, and the appropriate stellar metallicity. For comparison, the locations implied by the initial SME and SPC results are also shown (in each case with a triangle).

The stellar evolution modeling provides color indices that we compared against the measured values, as a sanity check. For each star we used the near-infrared magnitudes from the 2MASS Catalogue (Skrutskie et al. 2006), which are given in Table 5. These were converted to the photometric system of the models (ESO) using the transformations by Carpenter (2001). The resulting 2MASS-based color indices were all consistent (within 1σ) with the stellar model based color indices.

The distance for each star given in Table 5 was computed from the absolute K magnitude from the models and the 2MASS K_s magnitudes, ignoring extinction.

3.2. *Global modeling of the data*

We modeled simultaneously the HATNet photometry, the follow-up photometry, and the high-precision

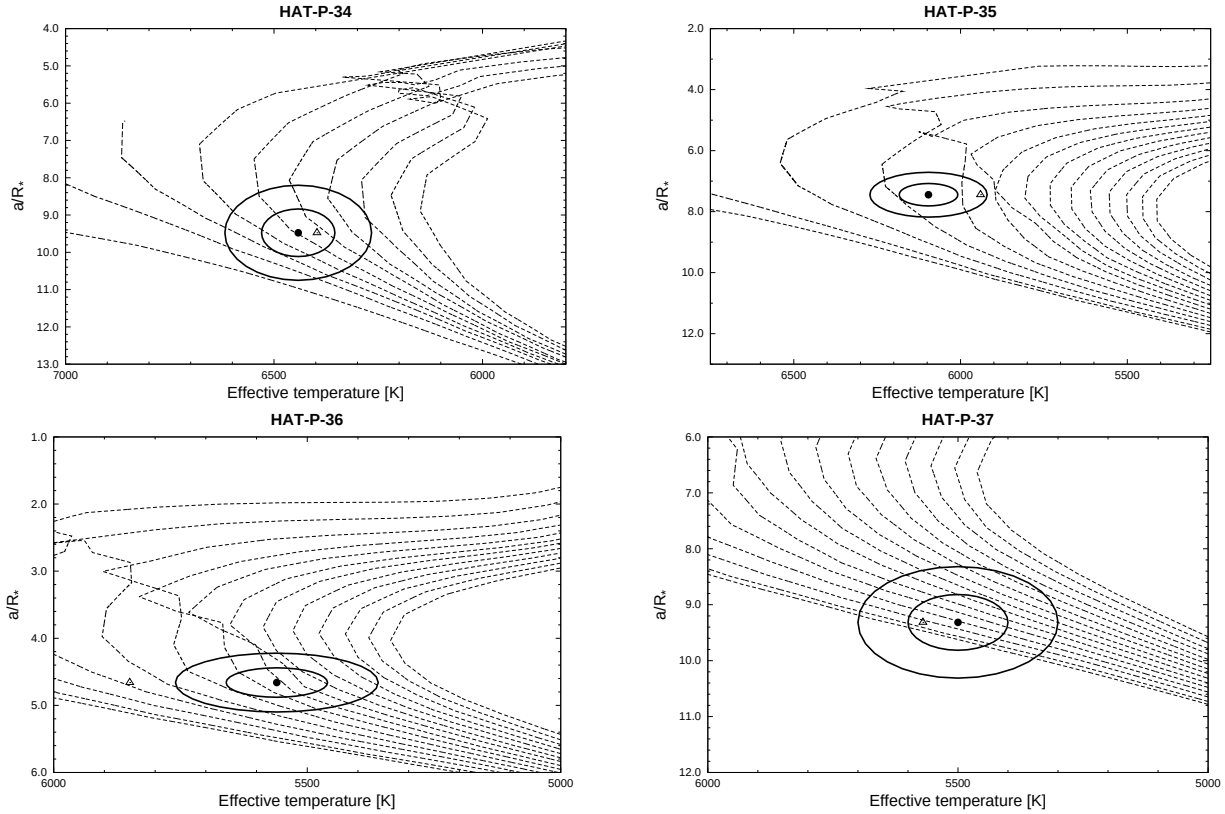

FIG. 10.— Comparison of the measured values of $T_{\rm eff\star}$ and $a/R_\star$ for HAT-P-34 (upper left), HAT-P-35 (upper right), HAT-P-36 (lower left) and HAT-P-37 (lower right) to model isochrones from Yi et al. (2001). The isochrones are generated for the measured metallicity of each star, and for ages of 0.5 Gyr and 1 to 3 Gyr in steps of 0.25 Gyr for HAT-P-34, and of 0.5 Gyr and 1 to 14 Gyr in steps of 1 Gyr for HAT-P-35, HAT-P-36 and HAT-P-37 (ages increase from left to right in each plot). The lines show the 1σ and 2σ confidence ellipses for the measured parameters. The initial values of $T_{\rm eff\star}$ and $a/R_\star$ from the initial spectroscopic and light curve analyses are represented with a triangle in each panel.

RV measurements using the procedures described by Bakos et al. (2010). Namely, the best fit was determined by a downhill simplex minimization, and was followed by a Monte-Carlo Markov Chain run to scan the parameter space around the minimum, and establish the errors Pál (2009b). For each system we used a Mandel & Agol (2002) transit model, together with the EPD and TFA trend-filters, to describe the follow-up light curves, a Mandel & Agol (2002) transit model for the HATNet light curve(s), and a Keplerian orbit using the formalism of Pál (2009a) for the RV curve(s). For HAT-P-34 we included a linear trend in the RV model, but find that it is only significant at the $\sim 2\sigma$ level; the planet and stellar parameters are changed by less than 1σ when the trend is not included in the fit. The parameters that we adopt for each system are listed in Table 6. In all cases we allow the eccentricity to vary so that the uncertainty on this parameter is propagated into the uncertainties on the other physical parameters, such as the stellar and planetary masses and radii; the observations of HAT-P-35b, HAT-P-36b, and HAT-P-37b are consistent with these planets being on circular orbits.

4. DISCUSSION

We have presented the discovery of four new transiting planets. Below we briefly discuss their properties.

4.1. *HAT-P-34b*

HAT-P-34b is a relatively massive $M_p = 3.328 \pm 0.211\,M_{\rm J}$ planet on a relatively long period ($P = 5.452654 \pm 0.000016\,{\rm d}$), eccentric ($e = 0.441 \pm 0.032$) orbit. There are only five known transiting planets with higher eccentricities (HAT-P-2b, $e = 0.5171 \pm 0.0033$, Pál et al. 2010; Bakos et al. 2007a; CoRoT-10b, $e = 0.53 \pm 0.04$, Bonomo et al. 2010; CoRoT-20b, $e = 0.562 \pm 0.013$, Deleuil et al. 2012; HD 17156b, $e = 0.669 \pm 0.008$, Madhusudhan & Winn 2009; and HD 80606b, $e = 0.9330 \pm 0.0005$, Hébrard et al. 2010), all of which have longer orbital periods than HAT-P-34b. Of these planets, HAT-P-2b is most similar in orbital period to HAT-P-34b, but it has a mass that is more than two times larger than that of HAT-P-34b. Two planets with masses, radii and equilibrium temperatures within 10% of the values of HAT-P-34b (assuming zero albedo and full heat redistribution) are CoRoT-18b (Hébrard et al. 2011) and WASP-32b (Maxted et al. 2010); however neither of these planets has a significant eccentricity.

HAT-P-34b is a promising target for measuring the Rossiter-McLaughlin effect (Rossiter 1924; McLaughlin 1924), since the host star is bright ($V = 10.16$), has a significant spin ($v \sin i = 24.0 \pm 0.5\,{\rm km\,s^{-1}}$), and the transit is moderately long ($T_{14} = 0.1455 \pm 0.0016\,{\rm days}$). Also, the transit is far from equatorial ($b = 0.336^{+0.099}_{-0.128}$), a configuration that is important for resolving the degeneracy between $v \sin i$ and λ, which is the sky-plane projected angle between the planetary orbital normal and the stellar spin axis. Winn et al. (2010) pointed out that

TABLE 5
Stellar parameters for HAT-P-34 through HAT-P-37

Parameter	**HAT-P-34** Value	**HAT-P-35** Value	**HAT-P-36** Value	**HAT-P-37** Value	Source
Spectroscopic properties					
$T_{\rm eff\star}$ (K)	6442 ± 88	6096 ± 88	5560 ± 100	5500 ± 100	Spec. Analysis.[a]
[Fe/H]	$+0.22 \pm 0.04$	$+0.11 \pm 0.08$	$+0.26 \pm 0.10$	$+0.03 \pm 0.10$	Spec. Analysis.
$v \sin i$ (km s^{-1})	24.0 ± 0.5	0.5 ± 0.5	3.58 ± 0.5	3.07 ± 0.5	Spec. Analysis.
$v_{\rm mac}$ (km s^{-1})	5.05	4.52	0.00	...	Spec. Analysis.
$v_{\rm mic}$ (km s^{-1})	0.85	0.85	0.00	...	Spec. Analysis.
$\gamma_{\rm RV}$ (km s^{-1})	-49.26 ± 0.30	40.95 ± 0.20	-16.29 ± 0.10	-20.53 ± 0.1	TRES
Photometric properties					
V (mag)	10.162 ± 0.073	12.46 ± 0.11	12.262 ± 0.068	13.23 ± 0.32	TASS,GSC[b]
$V-I_C$ (mag)	0.557 ± 0.12	0.662 ± 0.12	0.760 ± 0.13	$\cdots$	TASS
J (mag)	9.460 ± 0.022	11.358 ± 0.024	11.046 ± 0.027	12.092 ± 0.027	2MASS
H (mag)	9.322 ± 0.030	11.072 ± 0.023	10.723 ± 0.030	11.714 ± 0.032	2MASS
K_s (mag)	9.247 ± 0.023	11.030 ± 0.021	10.603 ± 0.021	11.667 ± 0.020	2MASS
Derived properties					
$M_\star$ ($M_\odot$)	1.392 ± 0.047	1.236 ± 0.048	1.022 ± 0.049	0.929 ± 0.043	YY+$a/R_\star$+Spec. Analysis. [c]
$R_\star$ ($R_\odot$)	$1.535^{+0.135}_{-0.102}$	1.435 ± 0.084	1.096 ± 0.056	$0.877^{+0.059}_{-0.044}$	YY+$a/R_\star$+Spec. Analysis
$\log g_\star$ (cgs)	4.21 ± 0.06	4.21 ± 0.04	4.37 ± 0.04	4.52 ± 0.05	YY+$a/R_\star$+Spec. Analysis
$L_\star$ ($L_\odot$)	$3.63^{+0.75}_{-0.51}$	$2.55^{+0.40}_{-0.30}$	1.03 ± 0.15	$0.62^{+0.11}_{-0.09}$	YY+$a/R_\star$+Spec. Analysis
M_V (mag)	3.32 ± 0.19	3.77 ± 0.15	4.83 ± 0.17	5.41 ± 0.19	YY+$a/R_\star$+Spec. Analysis
M_K (mag,ESO)	2.24 ± 0.17	2.43 ± 0.13	3.14 ± 0.12	3.64 ± 0.14	YY+$a/R_\star$+Spec. Analysis
Age (Gyr)	$1.7^{+0.4}_{-0.5}$	$3.5^{+0.8}_{-0.5}$	$6.6^{+2.9}_{-1.8}$	$3.6^{+4.1}_{-2.2}$	YY+$a/R_\star$+Spec. Analysis
Distance (pc)	257^{+22}_{-17}	535 ± 32	317 ± 17	411 ± 26	YY+$a/R_\star$+Spec. Analysis

[a] Based on the analysis of high resolution spectra. For HAT-P-34 and HAT-P-35 this corresponds to SME applied to iodine-free Keck/HIRES spectra, while for HAT-P-36 and HAT-P-37 this corresponds to SPC applied to the TRES spectra (Section 3.1). These parameters also have a small dependence on the iterative analysis incorporating the isochrone search and global modeling of the data, as described in the text.
[b] For HAT-P-34 through HAT-P-36 the value is taken from the TASS catalog, while for HAT-P-37 the value is taken from the GSC version 2.3.2.
[c] YY+$a/R_\star$+Spec. Analysis = Based on the YY isochrones (Yi et al. 2001), $a/R_\star$ as a luminosity indicator, and the spectroscopic analysis results.

hot Jupiters around stars with $T_{\rm eff\star} \gtrsim 6250\,K$ have a higher chance of being misaligned. Based on the effective temperature of the host star 6442 ± 88 K, we thus expect that HAT-P-34b has a higher chance of misalignment (note that this may not necessarily yield a non-zero λ, if HAT-P-34b's orbit is tilted along the line of sight). Alternatively, Schlaufman (2010) used a stellar rotation model and observed $v \sin i$ values to statistically identify TEP systems that may be misaligned along the line of sight, and concluded these preferentially occur at $M_\star > 1.2 M_\odot$. Based on the stellar mass alone ($1.39\,M_\odot$) we the chances for misalignment are increased.

4.2. *HAT-P-35b*

HAT-P-35b is a very typical $M_p = 1.054 \pm 0.033\,M_{\rm J}$, $R_p = 1.332 \pm 0.098\,R_{\rm J}$ planet on a $P = 3.646706 \pm 0.000021$ d orbit and with an equilibrium temperature of $T_{\rm eq} = 1581 \pm 45$ K (again, assuming zero albedo and full heat redistribution). There are four other planets with masses, radii and equilibrium temperatures that are all within 10% of the values for HAT-P-35b. These are HAT-P-5b (Bakos et al. 2007b), HAT-P-6b (Noyes et al. 2008), OGLE-TR-211b (Udalski et al. 2008), and WASP-26b (Smalley et al. 2010). The stellar effective temperature (6096 ± 88 K) is close to the assumed border-line between well-aligned and misaligned systems, making it an interesting system for testing the RM effect (with the caveat that $v \sin i$, and thus the expected amplitude of the anomaly, is low).

4.3. *HAT-P-36b*

HAT-P-36b is a very short period ($P = 1.327347 \pm 0.000003$ d) planet with a mass of $M_p = 1.832 \pm 0.099\,M_{\rm J}$, a radius of $R_p = 1.264 \pm 0.071\,R_{\rm J}$, and an equilibrium temperature of $T_{\rm eq} = 1823 \pm 55$ K. There are two other planets with masses, radii, and equilibrium temperatures within 10% of the values for HAT-P-36b: TrES-3b (O'Donovan et al. 2007) and WASP-3b (Pollacco et al. 2008).

4.4. *HAT-P-37b*

Like the preceding planets, HAT-P-37b also has very typical physical properties, with $M_p = 1.169 \pm 0.103\,M_{\rm J}$, $R_p = 1.178 \pm 0.077\,R_{\rm J}$, $P = 2.797436 \pm 0.000007$ d, and $T_{\rm eq} = 1271 \pm 47$ K. Three planets with masses, radii and equilibrium temperatures within 10% of the values for HAT-P-37b are HD 189733b (Bouchy et al. 2005), OGLE-TR-113b (Bouchy et al. 2004), and XO-5b (Burke et al. 2008). HAT-P-37 lies just outside of the field of view of the *Kepler* Space mission and is listed in the Kepler Input Catalog (KIC[14]) as KIC 12396036.

4.5. *On the eccentricity of HAT-P-34b*

According to Adams and Laughlin (2006), the eccentricity of a hot Jupiter's orbit decays both due to the tides on the star and due to the tides on the planet,

[14] http://www.cfa.harvard.edu/kepler/kic/kicindex.html

TABLE 6
Orbital and planetary parameters for HAT-P-34b through HAT-P-37b

Parameter	**HAT-P-34b** Value	**HAT-P-35b** Value	**HAT-P-36b** Value	**HAT-P-37b** Value
Light curve parameters				
P (days)	5.452654 ± 0.000016	3.646706 ± 0.000021	1.327347 ± 0.000003	2.797436 ± 0.000007
T_c (BJD) [a]	$2455431.59629 \pm 0.00055$	$2455578.66081 \pm 0.00050$	$2455565.18144 \pm 0.00020$	$2455642.14318 \pm 0.00029$
T_{14} (days) [a]	0.1455 ± 0.0016	0.1640 ± 0.0018	0.0923 ± 0.0007	0.0971 ± 0.0015
$T_{12} = T_{34}$ (days) [a]	0.0121 ± 0.0013	0.0162 ± 0.0017	0.0107 ± 0.0007	0.0153 ± 0.0013
$a/R_\star$	9.48 ± 0.64	7.45 ± 0.37	4.66 ± 0.22	$9.32^{+0.42}_{-0.57}$
$\zeta/R_\star$	14.99 ± 0.09	13.52 ± 0.09	24.51 ± 0.14	24.33 ± 0.18
$R_p/R_\star$	0.0801 ± 0.0026	0.0954 ± 0.0027	0.1186 ± 0.0012	0.1378 ± 0.0030
b^2	$0.113^{+0.080}_{-0.062}$	$0.128^{+0.078}_{-0.066}$	$0.097^{+0.057}_{-0.048}$	$0.255^{+0.044}_{-0.056}$
$b \equiv a\cos i/R_\star$	$0.336^{+0.099}_{-0.128}$	$0.357^{+0.092}_{-0.127}$	$0.312^{+0.078}_{-0.105}$	$0.505^{+0.041}_{-0.062}$
i (deg)	87.1 ± 1.2	87.3 ± 1.0	86.0 ± 1.3	$86.9^{+0.4}_{-0.5}$
Quadratic limb-darkening coefficients [b]				
c_1, i (linear term)	0.1785	0.2198	0.3142	0.3156
c_2, i (quadratic term)	0.3825	0.3587	0.3113	0.3032
c_1, z	0.1269	...	...	0.2477
c_2, z	0.3728	...	...	0.3082
RV parameters				
K ($\mathrm{m\,s^{-1}}$)	343.1 ± 21.3	120.7 ± 2.2	334.7 ± 14.5	177.7 ± 14.8
$e\cos\omega$ [c]	0.410 ± 0.031	-0.004 ± 0.013	-0.002 ± 0.032	-0.017 ± 0.039
$e\sin\omega$ [c]	0.156 ± 0.052	-0.017 ± 0.026	0.051 ± 0.040	0.007 ± 0.060
e	0.441 ± 0.032	0.025 ± 0.018	0.063 ± 0.032	0.058 ± 0.038
ω (deg)	20 ± 14	248 ± 93	95 ± 63	164 ± 84
$\dot{\gamma}$ ($\mathrm{m\,s^{-1}\,d^{-1}}$)	0.8683 ± 0.4719	...	...	...
RV jitter				
Keck/HIRES ($\mathrm{m\,s^{-1}}$)	56.0	3.7	...	...
Subaru/HDS ($\mathrm{m\,s^{-1}}$)	32.0	...	...	...
NOT/FIES ($\mathrm{m\,s^{-1}}$)	0.0	...	...	...
FLWO 1.5/TRES ($\mathrm{m\,s^{-1}}$)	...	...	33.6	25.8
Secondary eclipse parameters				
T_s (BJD)	2455435.721 ± 0.099	2455580.476 ± 0.030	2455565.844 ± 0.027	2455643.512 ± 0.070
$T_{s,14}$	0.1871 ± 0.0170	0.1596 ± 0.0076	0.1013 ± 0.0071	0.0981 ± 0.0083
$T_{s,12}$	0.0176 ± 0.0052	0.0156 ± 0.0019	0.0120 ± 0.0015	0.0153 ± 0.0029
Planetary parameters				
M_p (M_J)	3.328 ± 0.211	1.054 ± 0.033	1.832 ± 0.099	1.169 ± 0.103
R_p (R_J)	$1.197^{+0.128}_{-0.092}$	1.332 ± 0.098	1.264 ± 0.071	1.178 ± 0.077
$C(M_p, R_p)$ [d]	0.23	0.49	0.11	0.02
ρ_p ($\mathrm{g\,cm^{-3}}$)	2.40 ± 0.63	0.55 ± 0.11	1.12 ± 0.19	0.89 ± 0.19
$\log g_p$ (cgs)	3.76 ± 0.08	3.17 ± 0.06	3.45 ± 0.05	3.32 ± 0.07
a (AU)	0.0677 ± 0.0008	0.0498 ± 0.0006	0.0238 ± 0.0004	0.0379 ± 0.0006
T_eq (K)	1520 ± 60	1581 ± 45	1823 ± 55	1271 ± 47
Θ [e]	0.269 ± 0.029	0.064 ± 0.005	0.067 ± 0.005	0.081 ± 0.009
$\langle F \rangle$ ($10^9 \mathrm{erg\,s^{-1}\,cm^{-2}}$) [f]	$1.21^{+0.23}_{-0.16}$	$1.41^{+0.19}_{-0.14}$	2.49 ± 0.30	$0.589^{+0.102}_{-0.075}$

[a] T_c: Reference epoch of mid transit that minimizes the correlation with the orbital period. T_{14}: total transit duration, time between first to last contact; $T_{12} = T_{34}$: ingress/egress time, time between first and second, or third and fourth contact. Barycentric Julian dates (BJD) throughout the paper are calculated from Coordinated Universal Time (UTC).

[b] Values for a quadratic law, adopted from the tabulations by Claret (2004) according to the spectroscopic (SME) parameters listed in Table 5.

[c] Lagrangian orbital parameters derived from the global modeling, and primarily determined by the RV data.

[d] Correlation coefficient between the planetary mass M_p and radius R_p.

[e] The Safronov number is given by $\Theta = \frac{1}{2}(V_\mathrm{esc}/V_\mathrm{orb})^2 = (a/R_p)(M_p/M_\star)$ (see Hansen & Barman 2007).

[f] Incoming flux per unit surface area, averaged over the orbit.

with the tides on the planet dominating the circularization as long as the tidal quality factor of the planet (Q_P) is not much larger than the star's ($Q_\star$). Both of these factors are highly uncertain with various theoretical and observational constraints ranging over several orders of magnitude. In particular tidal circularization of main sequence stars (Claret & Cunha 1997; Meibom & Mathieu 2005; Zahn & Bouchet 1989; Zahn 1989) seem to indicate $10^5 \lesssim Q_\star \lesssim 10^6$. On the other hand, the discovery of extremely short period massive planets, the two most dramatic being WASP-18b (Hellier et al. 2009) and WASP-19b (Hellier et al. 2011), seems to be inconsistent with such efficient dissipation (Penev et al. in preparation), requiring much larger values $Q_\star \gtrsim 10^8$, which coincide well with the theoretical values derived by Penev & Sasselov (2011), who argue that binary stars and star-planet systems are subject to different modes of dissipation in the star. The tidal dissipation parameter in the planet has also been

the subject of many studies attempting to constrain it either from theory (Bodenheimer, Laughlin, & Lin 2003; Ogilvie & Lin 2004) or from the observed configuration of Jupiter's satellites (Goldreich & Soter 1966) giving $10^5 \lesssim Q_P \lesssim 10^7$.

With this in mind we conclude that the circularization of HAT-P-34b's orbit is likely dominated by the tidal dissipation in the planet and using $Q_P = 10^6$ and the expression for the tidal circularization timescale from Adams and Laughlin (2006), we estimate the eccentricity of HAT-P-34b should decay on the scale of 2Gyr, i.e. it is not in conflict with theoretical expectations. The possible outer companion indicated by the RV trend may also be responsible for pumping the eccentricity of the inner planet HAT-P-34b (see Correia et al. 2011 for a discussion).

Figure 11 shows HAT-P-34b on the orbital period–eccentricity plane of TEPs with well determined parameters (using our own compilation that attempts to keep up with various refinements to these parameters). It is apparent that eccentricity is correlated with orbital period and with planet mass, as expected from tidal theory. HAT-P-34b lies in a sparse position in these diagrams; for example, it has a high eccentricity for its period, the only similar planet being HAT-P-2b.

Figure 12 is a "tidal" plot (see Fig. 3 of Pont et al. 2011), showing TEPs with well measured properties in the a/R_p–$M_p/M_\star$ plane, using more data points (including the present discoveries) than Pont et al. (2011). Since $\tau_c = (4/63)Q_P\sqrt{(a^3/GM_\star}(a/R_P)^5 M_p/M_\star$, we expect planets with small relative semi-major axis (a/R_P) or planets with small relative mass ($M_p/M_\star$) to be circularized. This is indeed the case, as shown by the intensity (color) scale representing eccentricity. For hot Jupiters that migrate in by circularization of an initially very eccentric orbit, the expected "parking distance" is $\sim 2a_H$ (Ford and Rasio 2006), where a_H is the semi-major axis at which the radius of the planet equals its Hill radius. The thick solid line in Figure 12 shows this relation. A fairly good match for the dividing line between the circularized (denoted by black points) and eccentric (grey or color) points is at $a \approx 4a_H$ (marked with a thin solid line). This relation now includes very small mass Kepler discoveries. HAT-P-34b belongs to the sparse group of high relative semi-major axis (a/R_p) and massive extrasolar planets.

HATNet operations have been funded by NASA grants NNG04GN74G, NNX08AF23G. We acknowledge partial funding of the HATNet follow-up effort from NSF AST-1108686. We acknowledge partial support also from the Kepler Mission under NASA Cooperative Agreement NCC2-1390 (D.W.L., PI). G.K. thanks the Hungarian Scientific Research Foundation (OTKA) for support through grant K-81373. This research has made use of Keck telescope time granted through NOAO (program A289Hr) and NASA (N167Hr, N029Hr). This paper uses observations obtained with facilities of the Las Cumbres Observatory Global Telescope. Data presented in this paper are based on observations obtained at the HAT station at the Submillimeter Array of SAO, and HAT station at the Fred Lawrence Whipple Observatory of SAO. The authors wish to recognize and acknowledge the very significant cultural role and reverence that the summit of Mauna Kea has always had within the indigenous Hawaiian community. We are most fortunate to have the opportunity to conduct observations from this mountain.

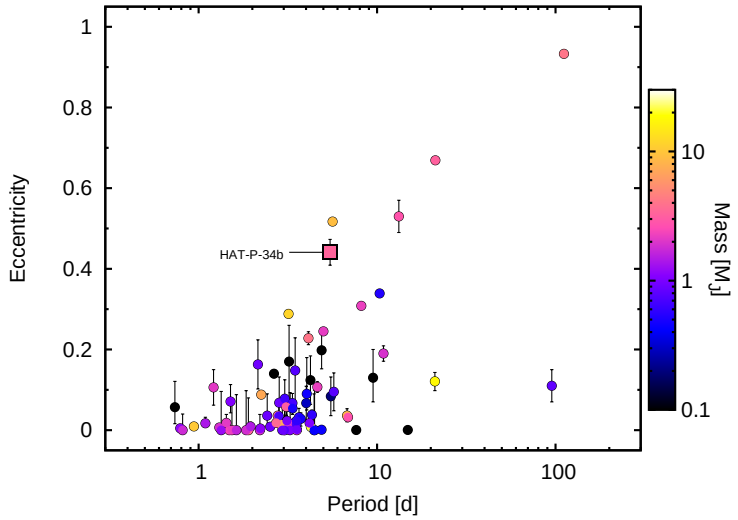

FIG. 11.— Orbital-period–eccentricity diagram of TEPs with eccentricity uncertainty less than 0.1. The color (greyscale shade) of the symbols indicates the mass of each planet. HAT-P-34b is labelled. As expected from tidal evolution theory, high eccentricity planets tend to have longer orbital periods and greater masses.

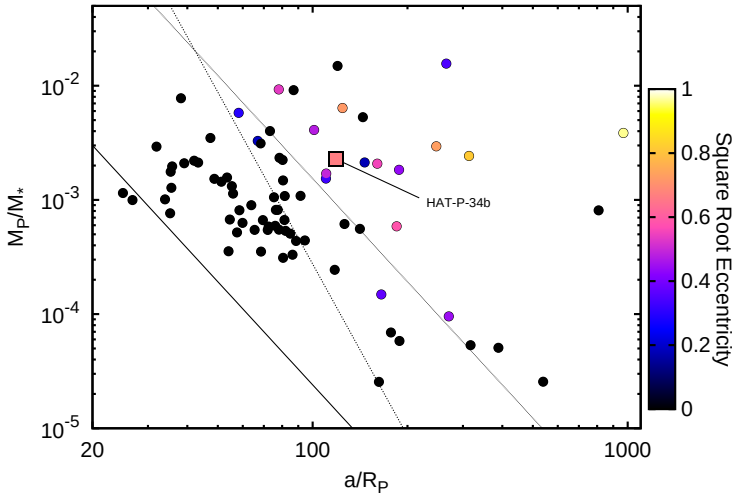

FIG. 12.— A "tidal" diagram following Fig. 3 of Pont et al. (2011). The color (greyscale shade) of the symbols indicates the eccentricity, we assume zero eccentricity for planets that have a measured eccentricity within 4σ of zero. The dotted line shows the locus of points with a circularization time-scale of 1 Gyr assuming small eccentricity, $Q_P = 10^6$, and $P = 3\,\mathrm{d}$. The thick solid line shows the relation $a = 2a_H$ where a_H is the semi-major axis at which the radius of the planet equals its Hill radius. The thin solid line shows $a = 4a_H$.

REFERENCES

Adams, F. C., & Laughlin, G. 2006, ApJ, 649, 1004
Bakos, G. Á., Noyes, R. W., Kovács, G., Stanek, K. Z., Sasselov, D. D., & Domsa, I. 2004, PASP, 116, 266
Bakos, G. Á., et al. 2007a, ApJ, 670, 826
Bakos, G. Á., et al. 2007b, ApJ, 671, L173
Bakos, G. Á., et al. 2010, ApJ, 710, 1724
Bodenheimer, P., Laughlin, G., & Lin, D. N. C. 2003, ApJ, 592, 555
Bonomo, A. S., et al. 2010, A&A, submitted
Borucki, W. J., et al. 2011, ApJ, 736, 19
Bouchy, F., Pont, F., Santos, N. C., Melo, C., Mayor, M., Queloz, D., & Udry, S. 2004, A&A, 421, L13
Bouchy, F., et al. 2005, A&A, 444, L15
Buchhave, L. A., et al. 2010, ApJ, 720, 1118
Burke, C. J., et al. 2008, ApJ, 686, 1331
Butler, R. P. et al. 1996, PASP, 108, 500
Carpenter, J. M. 2001, AJ, 121, 2851
Claret, A. 2004, A&A, 428, 1001
Cegla, H. M., et al. 2012, MNRAS, 421, L54
Claret, A.,& Cunha, N. C. S. 1997, A&A, 318, 187
Correia, A. C. M., Boué, G., & Laskar, J. 2011, ApJL in press, arXiv:1111.5486
Deleuil, M., et al. 2012, A&A, 538, A145
Djupvik, A. A., & Andersen, J. 2010, in "Highlights of Spanish Astrophysics V" eds. J. M. Diego, L. J. Goicoechea, J. I. González-Serrano, & J. Gorgas (Springer: Berlin), p. 211
Droege, T. F., Richmond, M. W., & Sallman, M. 2006, PASP, 118, 1666
Ford, E. B., & Rasio, F. A. 2006, ApJ, 638, L45
Fűrész, G. 2008, Ph.D. thesis, University of Szeged, Hungary
Goldreich, P., & Soter, S. 1966, Icarus, 5, 375
Hansen, B. M. S., & Barman, T. 2007, ApJ, 671, 861
Hartman, J. D., et al. 2009, ApJ, 706, 785
Hartman, J. D., Bakos, G. Á., Kipping, D. M., et al. 2011a, ApJ, 728, 138
Hartman, J. D., Bakos, G. Á., Torres, G., et al. 2011b, ApJ, 742, 59
Hébrard, G., Désert, J.-M., Díaz, R. F., et al. 2010, A&A, 516, A95
Hébrard, G., Evans, T. M., Alonso, R. 2011, A&A, 533, A130
Hellier, C., et al. 2009, Nature, 460, 1098
Hellier, C., Anderson, D. R., Collier-Cameron, A., Miller, G. R. M., Queloz, D., Smalley, B., Southworth, J., & Triaud, A. H. M. J. 2011, ApJ, 730, L31
Howard, A. W., et al. 2010, ApJ, 721, 1467
Howard, A. W., Marcy, G. W., Bryson, S. T., et al. 2011, arXiv:1103.2541
Isaacson, H., & Fischer, D. 2010, ApJ, 725, 875
Johnson, J. A., Winn, J. N., Albrecht, S., Howard, A. W., Marcy, G. W., & Gazak, J. Z. 2009, PASP, 121, 1104
Johnson, J. A., Winn, J. N., Bakos, G. Á., et al. 2011, ApJ, 735, 24
Kovács, G., Zucker, S., & Mazeh, T. 2002, A&A, 391, 369
Kovács, G., Bakos, G. Á., & Noyes, R. W. 2005, MNRAS, 356, 557
Kovács, G., Bakos, G. á., Hartman, J. D., et al. 2010, ApJ, 724, 866
Kurucz, R. L. 2005, Memorie della Societa Astronomica Italiana Supplementi, 8, 14
Lasker, B. M., et al. 2008, AJ, 136, 735
Latham, D. W., et al. 2009, ApJ, 704, 1107
Latham, D. W., Rowe, J. F., Quinn, S. N., et al. 2011, ApJ, 732, L24
Lissauer, J. J., Ragozzine, D., Fabrycky, D. C., et al. 2011, ApJS, 197, 8
Madhusudhan, N., & Winn, J. N. 2009, ApJ, 693, 784
Makarov, V. V., Beichman, C. A., Catanzarite, J. H., Fischer, D. A., Lebreton, J., Malbet, F., & Shao, M. 2009, ApJ, 707, L73
Mandel, K., & Agol, E. 2002, ApJ, 580, L171
Marcy, G. W., & Butler, R. P. 1992, PASP, 104, 270
Martínez-Arnáiz, R., Maldonado, J., Montes, D., Eiroa, C., & Montesinos, B. 2010, A&A, 520, A79
Maxted, P. F. L, Anderson, D. R., Collier Cameron, A., et al. 2010, PASP, 122, 1465
McLaughlin, D. B. 1924, ApJ, 60, 22
Meibom, S., & Mathieu, R. D. 2005, ApJ, 620, 970
Noguchi, K., et al. 2002, PASJ, 54, 855
Noyes, R. W., Hartmann, L. W., Baliunas, S. L., Duncan, D. K., & Vaughan, A. H. 1984, ApJ, 279, 763
Noyes, R. W., et al. 2008, ApJ, 673, L79
O'Donovan, F. T., et al. 2007, ApJ, 663, L37
Ogilvie, G. I., & Lin, D. N. C. 2004, ApJ, 610, 477
Pál, A. 2009a, MNRAS, 396, 1737
Pál, A. 2009b, PhD thesis, Department of Astronomy, Eőtvős Loránd University, arXiv:0906.3486
Pál, A., et al. 2010, MNRAS, 401, 2665
Penev, K., & Sasselov, D. 2011, ApJ, 731, 67
Pollacco, D., et al. 2008, MNRAS, 385, 1576
Pont, F., Husnoo, N., Mazeh, T., & Fabrycky, D. 2011, MNRAS, 414, 1278
Queloz, D. et al. 2001, A&A, 379, 279
Quinn, S. N., et al. 2010, ApJ, submitted, arXiv:1008.3565
Rauer, H. 2011, in "Detection and Dynamics of Transiting Exoplanets, St. Michel l'Observatoire, France", Edited by F. Bouchy; R. Díaz; C. Moutou; EPJ Web of Conferences, Volume 11, id.07001, 11, 7001
Rossiter, R. A. 1924, ApJ, 60, 15
Saar, S. H., Hatzes, A., Cochran, W., & Paulson, D. 2003, The Future of Cool-Star Astrophysics: 12th Cambridge Workshop on Cool Stars, Stellar Systems, and the Sun , 12, 694
Sato, B., Kambe, E., Takeda, Y., Izumiura, H., & Ando, H. 2002, PASJ, 54, 873
Sato, B., et al. 2005, ApJ, 633, 465
Schlaufman, K. C. 2010, ApJ, 719, 602
Schneider, J., Dedieu, C., Le Sidaner, P., Savalle, R., & Zolotukhin, I. 2011, A&A, 532, A79
Skrutskie, M. F., et al. 2006, AJ, 131, 1163
Smalley, B., Anderson, D. R., Collier Cameron, A., et al. 2010, A&A, 520, A56
Sozzetti, A. et al. 2007, ApJ, 664, 1190
Torres, G. et al. 2007, ApJ, 666, 121
Udalski, A., et al. 2008, A&A, 482, 299
Valenti, J. A., & Fischer, D. A. 2005, ApJS, 159, 141
Valenti, J. A., & Piskunov, N. 1996, A&AS, 118, 595
Vaughan, A. H., Preston, G. W., & Wilson, O. C. 1978, PASP, 90, 267
Vogt, S. S. et al. 1994, Proc. SPIE, 2198, 362
Winn, J. N., Fabrycky, D., Albrecht, S., & Johnson, J. A. 2010, ApJ, 718, L145
Wright, J. T., et al. 2011, PASP, 123, 412
Yi, S. K. et al. 2001, ApJS, 136, 417
Zahn, J.-P., & Bouchet, L. 1989, A&A, 223, 112
Zahn, J.-P. 1989, A&A, 220, 112
Wright, J. T. 2005, PASP, 117, 657

APPENDIX

SPECTROSCOPIC AND PHOTOMETRIC DATA

The following tables present the spectroscopic data (radial velocities, bisector spans, and activity index measurements) and high precision photometric data for the four planets presented in this paper.

TABLE 7
Relative radial velocities, bisector spans, and activity index measurements of HAT-P-34.

BJD (2,454,000+)	RV[a] ($\mathrm{m\,s^{-1}}$)	σ_{RV}[b] ($\mathrm{m\,s^{-1}}$)	BS ($\mathrm{m\,s^{-1}}$)	σ_{BS} ($\mathrm{m\,s^{-1}}$)	S[c]	Phase	Instrument
1339.92722	−158.62	50.92	···	···	···	0.188	Subaru
1339.93516	−201.37	57.36	···	···	···	0.190	Subaru
1339.94290	−204.06	44.53	···	···	···	0.191	Subaru
1341.11630	−246.80	47.11	···	···	···	0.406	Subaru
1341.12058	−204.87	47.32	···	···	···	0.407	Subaru
1341.12485	−193.24	43.00	···	···	···	0.408	Subaru
1374.12069	−196.46	11.37	−2.85	6.57	0.176	0.459	Keck
1374.85735	···	···	−9.20	4.18	0.173	0.594	Keck
1374.86800	−80.49	11.89	−25.52	9.34	0.176	0.596	Keck
1375.95203	285.94	10.24	−15.73	4.46	0.178	0.795	Keck
1378.12823	−265.18	12.71	−13.52	7.86	0.174	0.194	Keck
1379.07458	−226.26	12.73	−10.85	3.72	0.176	0.368	Keck
1379.56536	−162.68	61.60	···	···	···	0.458	FIES
1380.13344	−135.85	13.51	60.87	20.44	0.180	0.562	Keck
1380.49378	3.45	58.70	···	···	···	0.628	FIES
1381.11125	110.87	14.71	−9.04	12.64	0.175	0.741	Keck
1381.55600	269.57	46.50	···	···	···	0.823	FIES
1383.47949	−108.72	56.00	···	···	···	0.176	FIES
1384.48968	−173.76	50.60	···	···	···	0.361	FIES
1400.85414	−141.78	15.43	27.38	7.53	0.167	0.362	Keck
1403.82567	497.16	15.18	38.35	6.14	0.173	0.907	Keck
1404.83902	4.37	14.05	0.79	7.25	0.174	0.093	Keck
1415.04513	310.06	14.03	2.76	8.29	0.168	0.965	Keck
1423.66787	−115.78	78.50	···	···	···	0.546	FIES
1424.64318	41.31	139.40	···	···	···	0.725	FIES
1425.57489	474.54	48.70	···	···	···	0.896	FIES
1426.64513	−154.35	57.60	···	···	···	0.092	FIES
1464.85484	−99.38	15.03	−11.41	11.10	0.164	0.100	Keck
1465.94874	−249.34	13.70	−19.33	6.92	0.163	0.300	Keck
1467.71998	0.98	13.61	−12.70	8.00	0.164	0.625	Keck

Note. — Note that for the iodine-free template exposures we do not measure the RV but do measure the BS and S index. Such template exposures can be distinguished by the missing RV value.

[a] The zero-point of these velocities is arbitrary. An overall offset γ_{rel} fitted to these velocities in Section 3.2 has *not* been subtracted.

[b] Internal errors excluding the component of astrophysical jitter considered in Section 3.2.

[c] Chromospheric activity index, calibrated to the scale of Vaughan, Preston & Wilson (1978).

TABLE 8
Relative radial velocities, bisector spans, and activity index measurements of HAT-P-35.

BJD (2,454,000+)	RV[a] ($\mathrm{m\,s^{-1}}$)	σ_{RV}[b] ($\mathrm{m\,s^{-1}}$)	BS ($\mathrm{m\,s^{-1}}$)	σ_{BS} ($\mathrm{m\,s^{-1}}$)	S[c]	Phase	Instrument
1466.12094	−92.77	2.40	−7.06	3.64	0.129	0.139	Keck
1468.11371	111.39	1.86	4.37	2.92	0.129	0.686	Keck
1468.12932	···	···	0.45	2.76	0.129	0.690	Keck
1470.12970	−118.71	2.72	2.26	2.07	0.124	0.239	Keck
1482.73469[d]	106.37	10.20	7.70	9.60	···	0.695	FIES
1483.74899[d]	39.07	10.70	−17.40	6.50	···	0.973	FIES
1486.74544[d]	97.37	8.50	8.90	8.30	···	0.795	FIES
1488.74737[d]	−152.93	16.90	24.70	17.20	···	0.344	FIES
1490.72460[d]	78.27	8.50	−23.80	6.40	···	0.886	FIES
1501.03468	117.01	2.39	9.98	2.63	0.127	0.713	Keck
1523.09695	126.39	2.09	0.65	4.88	0.134	0.763	Keck
1529.15460	−55.78	2.32	−11.07	2.00	0.129	0.424	Keck
1545.14866	103.29	3.12	9.13	3.56	0.125	0.810	Keck

Note. — Note that for the iodine-free template exposures we do not measure the RV but do measure the BS and S index. Such template exposures can be distinguished by the missing RV value.

[a] The zero-point of these velocities is arbitrary. An overall offset γ_{rel} fitted to these velocities in Section 3.2 has *not* been subtracted.

[b] Internal errors excluding the component of astrophysical jitter considered in Section 3.2.

[c] Chromospheric activity index, calibrated to the scale of Vaughan, Preston & Wilson (1978).

[d] The FIES/NOT observations of HAT-P-35 were not used in the analysis, see the footnote to Table 4. Transit ingress began during the hour-long exposure obtained at phase 0.973, and the exposure obtained at phase 0.344 has a low S/N ratio and was obtained during morning twilight.

TABLE 9
Relative radial velocities, bisector spans, and activity index measurements of HAT-P-36.

BJD (2,454,000+)	RV[a] ($\mathrm{m\,s^{-1}}$)	σ_{RV}[b] ($\mathrm{m\,s^{-1}}$)	BS ($\mathrm{m\,s^{-1}}$)	σ_{BS} ($\mathrm{m\,s^{-1}}$)	Phase
1547.02139	−206.37	22.40	20.50	15.80	0.319
1550.04236	200.83	22.80	−11.40	21.60	0.594
1554.99394	−293.87	11.40	−7.50	7.50	0.325
1556.05388	−237.67	7.40	3.20	7.70	0.123
1557.05533	240.83	24.60	5.10	18.40	0.878
1558.95741	−355.47	10.50	4.30	8.70	0.311
1559.99613	−199.97	17.70	−14.10	17.40	0.093
1576.04204	−326.97	16.70	···	···	0.182
1576.91790	331.53	14.40	···	···	0.842
1578.04243	265.83	7.40	···	···	0.689
1579.96119	−277.57	9.00	···	···	0.135
1580.92488	257.33	12.40	···	···	0.861

[a] The zero-point of these velocities is arbitrary. An overall offset γ_{rel} fitted to these velocities in Section 3.2 has *not* been subtracted.
[b] Internal errors excluding the component of astrophysical jitter considered in Section 3.2.

TABLE 10
Relative radial velocities, bisector spans, and activity index measurements of HAT-P-37.

BJD (2,454,000+)	RV[a] ($\mathrm{m\,s^{-1}}$)	σ_{RV}[b] ($\mathrm{m\,s^{-1}}$)	BS ($\mathrm{m\,s^{-1}}$)	σ_{BS} ($\mathrm{m\,s^{-1}}$)	Phase
1646.92799	146.43	35.50	26.20	16.30	0.710
1648.01278	−111.17	24.60	−28.00	16.30	0.098
1648.91342	−88.77	23.20	0.60	22.20	0.420
1649.89870	172.53	29.40	8.30	24.10	0.772
1650.96241	−102.97	17.50	12.30	16.90	0.153
1652.92638	128.33	26.30	−13.70	15.00	0.855
1656.98738	−238.57	12.80	−28.70	23.90	0.306
1658.96338	−19.87	20.90	−9.00	17.00	0.013
1663.90569	169.23	20.60	−5.60	15.10	0.779
1664.91140	−163.77	25.40	−28.30	19.50	0.139
1665.91961	62.93	32.60	−29.50	16.80	0.499
1671.84933	125.23	35.30	47.40	27.20	0.619
1698.79464	−143.97	25.00	48.00	16.20	0.251

[a] The zero-point of these velocities is arbitrary. An overall offset γ_{rel} fitted to these velocities in Section 3.2 has *not* been subtracted.
[b] Internal errors excluding the component of astrophysical jitter considered in Section 3.2.

TABLE 11
High-precision differential photometry of HAT-P-34.

BJD (2,400,000+)	Mag[a]	σ_{Mag}	Mag(orig)[b]	Filter
55338.79359	0.00011	0.00080	10.12720	i
55338.79427	−0.00108	0.00080	10.12640	i
55338.79494	0.00263	0.00080	10.12910	i
55338.79563	−0.00041	0.00080	10.12660	i
55338.79633	0.00158	0.00080	10.12850	i
55338.79701	0.00036	0.00079	10.12720	i
55338.79769	−0.00243	0.00079	10.12440	i
55338.79837	−0.00305	0.00079	10.12340	i
55338.79905	0.00184	0.00079	10.12940	i
55338.79969	0.00187	0.00079	10.12900	i

Note. — This table is available in a machine-readable form in the online journal. A portion is shown here for guidance regarding its form and content.
[a] The out-of-transit level has been subtracted. These magnitudes have been subjected to the EPD and TFA procedures, carried out simultaneously with the transit fit.
[b] Raw magnitude values without application of the EPD and TFA procedures.

TABLE 12
High-precision differential photometry of HAT-P-35.

BJD (2,400,000+)	Mag[a]	$\sigma_{\rm Mag}$	Mag(orig)[b]	Filter
55578.68612	0.00996	0.00115	11.35390	i
55578.68766	0.01222	0.00104	11.35670	i
55578.68921	0.01205	0.00101	11.35720	i
55578.69075	0.00983	0.00097	11.35550	i
55578.69228	0.01193	0.00099	11.35670	i
55578.69383	0.01274	0.00113	11.35760	i
55578.69504	0.01155	0.00113	11.35620	i
55578.69622	0.01243	0.00115	11.35790	i
55578.69742	0.01049	0.00114	11.35540	i
55578.69863	0.00960	0.00114	11.35430	i

Note. — This table is available in a machine-readable form in the online journal. A portion is shown here for guidance regarding its form and content.

[a] The out-of-transit level has been subtracted. These magnitudes have been subjected to the EPD and TFA procedures, carried out simultaneously with the transit fit.

[b] Raw magnitude values without application of the EPD and TFA procedures.

TABLE 13
High-precision differential photometry of HAT-P-36.

BJD (2,400,000+)	Mag[a]	$\sigma_{\rm Mag}$	Mag(orig)[b]	Filter
55555.84870	0.00292	0.00081	10.95490	i
55555.85050	0.00957	0.00083	10.96050	i
55555.85205	0.00817	0.00078	10.96100	i
55555.85362	0.01416	0.00079	10.96370	i
55555.85516	0.01203	0.00079	10.96260	i
55555.85671	0.01521	0.00079	10.96600	i
55555.85826	0.01690	0.00078	10.96760	i
55555.85981	0.01833	0.00079	10.96870	i
55555.86135	0.01590	0.00078	10.96410	i
55555.86292	0.01733	0.00078	10.96540	i

Note. — This table is available in a machine-readable form in the online journal. A portion is shown here for guidance regarding its form and content.

[a] The out-of-transit level has been subtracted. These magnitudes have been subjected to the EPD and TFA procedures, carried out simultaneously with the transit fit.

[b] Raw magnitude values without application of the EPD and TFA procedures.

TABLE 14
High-precision differential photometry of HAT-P-37.

BJD (2,400,000+)	Mag[a]	$\sigma_{\rm Mag}$	Mag(orig)[b]	Filter
55616.96855	0.02527	0.00133	12.41350	i
55616.97081	0.02387	0.00135	12.41200	i
55616.97308	0.02220	0.00133	12.41020	i
55616.97540	0.02311	0.00131	12.41290	i
55616.97774	0.02297	0.00132	12.41110	i
55616.97986	0.02149	0.00133	12.40940	i
55616.98176	0.02186	0.00133	12.40980	i
55616.98366	0.01909	0.00131	12.40740	i
55616.98555	0.02301	0.00132	12.41180	i
55616.98744	0.02165	0.00129	12.40910	i

Note. — This table is available in a machine-readable form in the online journal. A portion is shown here for guidance regarding its form and content.

[a] The out-of-transit level has been subtracted. These magnitudes have been subjected to the EPD and TFA procedures, carried out simultaneously with the transit fit.

[b] Raw magnitude values without application of the EPD and TFA procedures.